frontiers in Catalysis

ORIGINAL RESEARCH
published: 13 April 2021
doi: 10.3389/fctls.2021.669260

Tailoring Noble Metal-Free Ti@TiO_2 Photocatalyst for Boosting Photothermal Hydrogen Production

Sara El Hakim[1], *Tony Chave*[1], *Amr A. Nada*[2,3], *Stéphanie Roualdes*[2] *and Sergey I. Nikitenko*[1]*

[1] ICSM, Univ. Montpellier, UMR 5257, CEA-CNRS-UM-ENSCM, Bagnols-sur-Cèze, France, [2] Institut Européen des Membranes, UMR 5635, Univ. Montpellier, ENSCM, CNRS, Montpellier, France, [3] Department of Analysis and Evaluation, Egyptian Petroleum Research Institute, Cairo, Egypt

In this work, we provide new insights into the design of Ti@TiO_2 photocatalyst with enhanced photothermal activity in the process of glycerol reforming. Ti@TiO_2 nanoparticles have been obtained by sonohydrothermal treatment of titanium metal nanoparticles in pure water. Variation of sonohydrothermal temperature allows controlling nanocrystalline TiO_2 shell on Ti^0 surface. At $100 < T < 150°C$ formation of TiO_2 NPs occurs mostly by crystallization of Ti(IV) amorphous species and oxidation of titanium suboxide Ti_3O presented at the surface of Ti^0 nanoparticles. At $T > 150°C$, TiO_2 is also formed by oxidation of Ti^0 with overheated water. Kinetic study highlights the importance of TiO_2 nanocrystalline shell for H_2 generation. Electrochemical impedance spectroscopy points out more efficient electron transfer for Ti@TiO_2 nanoparticles in correlation with photocatalytic data. The apparent activation energy, $E_a = (25–31) \pm 5$ $kJ{\cdot}mol^{-1}$, assumes that photothermal effect arises from diffusion of glycerol oxidation intermediates or from water dynamics at the surface of catalyst. Under the heating, photocatalytic H_2 emission is observed even in pure water.

Keywords: photocatalysis, hydrogen, nanomaterials, titanium suboxide, sonohydrothermal

OPEN ACCESS

Edited by:
Maria Olea,
University of Cambridge,
United Kingdom

Reviewed by:
Chuncai Kong,
Xi'an Jiaotong University, China
Nageswara Rao Peela,
Indian Institute of Technology
Guwahati, India

***Correspondence:**
Sergey I. Nikitenko
serguei.nikitenko@cea.fr

Specialty section:
This article was submitted to Heterogeneous Catalysis, a section of the journal Frontiers in Catalysis

Received: *18 February 2021*
Accepted: *18 March 2021*
Published: *13 April 2021*

Citation:
El Hakim S, Chave T, Nada AA, Roualdes S and Nikitenko SI (2021) Tailoring Noble Metal-Free Ti@TiO_2 Photocatalyst for Boosting Photothermal Hydrogen Production. Front. Catal. 1:669260. doi: 10.3389/fctls.2021.669260

INTRODUCTION

Hydrogen is a clean fuel that, when consumed in a fuel cell, yields only water. Today, 95% of hydrogen is produced from fossil fuels, such as natural gas and oil (Baykara, 2018). Conversion of solar energy into hydrogen via photocatalytic splitting of water is an alternative sustainable process of paramount interest for clean energy storage (Ma et al., 2014; Ghosh, 2018). In this view, preparation of stable and non-toxic catalysts from non-precious elements showing high photocatalytic activity under solar light irradiation is of great importance. Among a wide variety of catalysts, titanium oxide, TiO_2, has been recognized as one of the most popular photocatalysts. However, TiO_2 can absorb only around 6% of the sunlight, owing to a quite large bandgap of 3.2 eV for anatase phase (Ghosh, 2018). Another serious bottleneck of TiO_2 is a rapid electron-hole recombination leading to the decrease in photocatalytic activity. Therefore, tremendous efforts have been undertaken to narrow bandgap of TiO_2 and to improve photogenerated charge separation. The recent advances in photocatalysis with TiO_2-based materials pointed out several strategies of TiO_2 bandgap engineering: doping of TiO_2 with cations or anions, codoping with cations and anions, self-doping of TiO_2 with Ti^{3+}, and surface sensitization with organic dyes or transition metal complexes (Ma et al., 2014).

On the other hand, fabrication of TiO_2 heterojunctions with other semiconductors, anatase-rutile phase junctions, and TiO_2 loading with cocatalysts, often noble metal nanoparticles, allows to minimize electron-hole recombination during the photocatalytic process (Ghosh, 2018).

Design of catalyst morphology is another important strategy to reach maximal photocatalytic activity. Core-shell nanoparticles have attracted a great deal of attention as promising photocatalysts for hydrogen production due to the synergism between the cores and shells and/or new properties providing by the interactions between the cores and shells (Gawande et al., 2015). Recently, we reported strong photothermal effect in the process of photocatalytic hydrogen production from the aqueous solutions of methanol and glycerol in the presence of noble metal-free Ti@TiO_2 core-shell nanoparticles (NPs) (Nikitenko et al., 2015, Nikitenko et al., 2018). It is noteworthy that the combination of photonic and thermal energy could be very beneficial for efficient solar energy harvesting (Ma et al., 2020). However, the mechanism of Ti@TiO_2 formation and the influence of TiO_2 nanocrystalline shell on the photocatalytic performance have not been examined. In this work, we applied simultaneous ultrasonic and hydrothermal treatment, called sonohydrothermal treatment (SHT), for the preparation of Ti@TiO_2 NPs with controlled Ti/TiO_2 ratio. SHT is an emerging environmentally benign technique effective for the synthesis of nanocrystalline materials with enhanced properties (Nikitenko et al., 2015, Nikitenko et al., 2018, Cau et al., 2013). Glycerol reforming was used to evaluate the photothermal performance of prepared Ti@TiO_2 NPs. Glycerol is a low-cost biomass derivative suitable for hydrogen production (Shimura and Yosida, 2011). Furthermore, quite high boiling point of glycerol (290°C) allows to study the photothermal effect in a large temperature range. In addition, Ti@TiO_2 NPs have been studied for the first time using electrochemical impedance spectroscopy (EIS). Combination of characterization techniques and kinetic study provided new insights into the mechanism of hydrogen formation and the origin of photothermal effect in studied system.

MATERIALS AND METHODS

Catalyst Preparation

The commercially available titanium nanopowder (Nanostructured & Amorphous Materials, Inc. Ti, 99%) is an air-sensitive material and it was stored in the argon-filled glove box prior use. Stable Ti@TiO_2 NPs were prepared by SHT treatment of Ti nanopowder in pure water (Milli-Q 18.2 MΩ·cm at 25°C). The SHT reactor is shown in **Supplementary Figure 1** and described previously (Cau et al., 2013; Nikitenko et al., 2015, 2018). In a typical experiment, 2 g of air passivated Ti nanopowder was dispersed in 50 mL of water using ultrasonic bath, placed in SHT reactor and heated at selected temperatures in the range of T = 100–214°C (autogenic pressure P = 1.0–19.0 bar) under simultaneous ultrasonic treatment (f = 20 kHz, P_{ac} = 17 W) for 3 h. After cooling, the treated NPs were recovered by centrifugation, washed with pure water and dried at room temperature under reduced pressure.

Catalyst Characterization

Powder X-Ray Diffraction (XRD) diagrams were recorded with the use of a Bruker D8 Advance X-ray diffractometer equipped with a linear Lynx-eye detector (Cu $K\alpha_{1,2}$ radiation, $\lambda = 1.54184$ Å). XRD patterns were collected between 10 and 90° ($\theta - 2\theta$ mode) at room temperature, with a step size of $\Delta(2\theta) = 0.02°$ and a counting time of 1.8 s·step^{-1}. Quantitative phase analysis was performed by Rietveld refinement with the phase detection limit about 5% (León-Reina et al., 2016). High-resolution transmission electron microscopic (HRTEM) and scanning transmission electron microscopic (STEM) measurements coupled with EDX mapping (SDD Oxford detector) were performed using a Jeol 2200FS (200 kV) microscope. XPS analysis was achieved with an ESCALAB 250 Thermo Electron device operated under ultra-high vacuum. The excitation source was a monochromatic source (Al-K_α, $\varepsilon = 1486.6$ eV) with a ca. 0.4 mm^2 X-ray spot. The pass energy was fixed at 20 eV. The photoelectron spectra were calibrated using the Au 4f 7/2 (83.9 ± 0.1 eV) and Cu 2p 3/2 (932.8 ± 0.1 eV) photoelectron lines. The XPS spectra were treated using AVANTAGE software. The binding energy scale was established by referencing the adventitious C 1 s peak at 284.8 eV. The reflectance spectra were recorded in $BaSO_4$ pellets with a Shimadzu UV-3600 spectrophotometer. Thermogravimetric analysis (TGA) was performed by means of TGA-DTA/DSC Setsys Evolution (Setaram Instrumentation) device in air flow (900°C, 10°C·min^{-1}). The concentration of titanium species in solution after photolysis was measured using SPECTRO ARCOS ICP-OES instrument (detection limit ∼ 0.1 ppm).

Electrochemical Measurements

Electrochemical Impedance Spectroscopy (EIS) was studied at dark conditions in the frequency range from 0.1 to 100 kHz with an AC amplitude 10 mV. The electrolytic cell was filled with 1 M KOH and bubbled with Ar for 20 min prior the measurements. Silver/silver chloride (Ag/AgCl) and platinum (Pt) were used as the reference electrode and counter electrode, respectively. The working electrode was prepared by ultrasonic dispersion of the synthesized photocatalyst (5 mg) in the mixture of 1 mL isopropanol (VWR, ≥99.7%) and 40 μL Nafion (Aldrich, 5 wt% lower aliphatic alcohols, 15–20% water). Then 5 μL of the photocatalyst suspension was deposited onto glassy carbon electrode.

Photothermal Hydrogen Formation

The photocatalytic study was performed in aqueous glycerol (99% Sigma-Aldrich) solutions using a thermostated gas-flow cell made from a borosilicate glass and adapted to mass spectrometric analysis of the outlet gases. The image of the photocatalytic cell is shown in **Supplementary Figure 2**. In a typical run, 7.8 mg of photocatalyst was ultrasonically dispersed in 65 mL of aqueous glycerol solution and placed into the photoreactor. Photolysis was carried out using a white light of ASB-XE-175 W xenon lamp equipped with ozone blocking coatings. The lamp was placed at 8 cm away from the reactor and the light power at this distance was measured by X1-1 Optometer (Gigahertz-Optik) using UV-3710-4 (300–420 nm) and RW-3705-4 (400–1,100 nm) calibrated

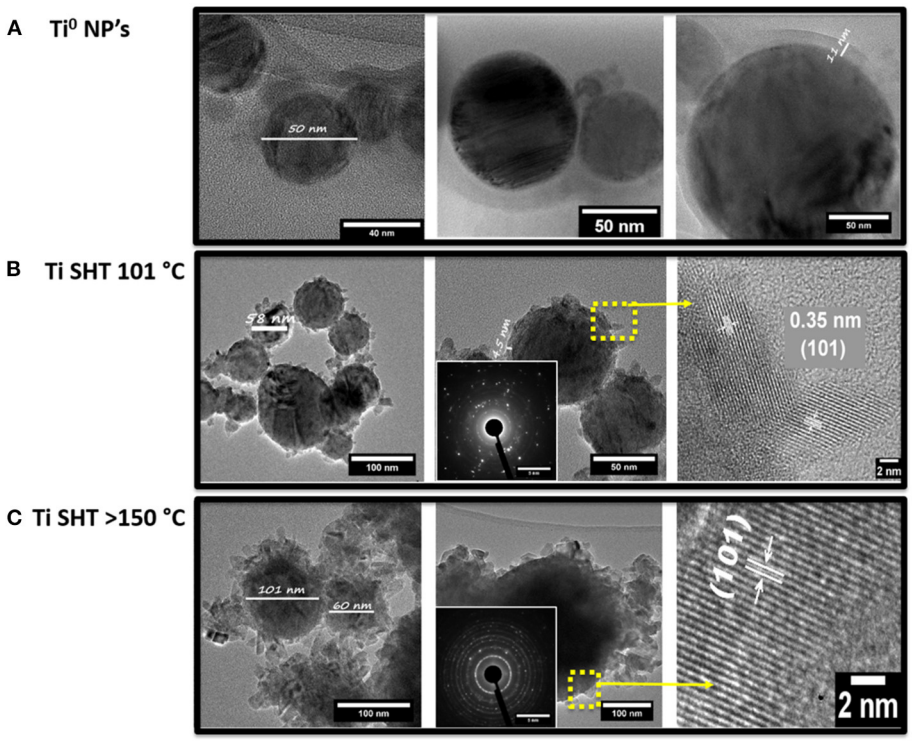

FIGURE 1 | Typical TEM images of initial Ti particles **(A)**, SHT-treated particles in water at 101°C **(B)**, and >150°C **(C)**. The distance of 0.35 nm corresponds to (101) plane of TiO_2 anatase.

detectors. The obtained values of light power were equal to 8.9 and 0.6 W for vis/NIR and UV spectral ranges respectively, which provides the close spectral match to solar spectra. The solutions inside the reactor were stirred continuously and the temperature was gradually increased up to 95°C during photolysis. The Ar gas flow through the reactor was kept constant at 58 mL·min^{-1} and controlled by a volumetric flowmeter. The gaseous products in the outlet gas were analyzed using a Thermo Scientific PRIMA BT mass spectrometer. The H_2 formation rate was quantified using external calibration curves prepared with standard gas mixtures in argon (Messer). The water vapors were trapped with molecular sieve (Sigma-Aldrich, 5 Å) prior to mass spectrometric analysis.

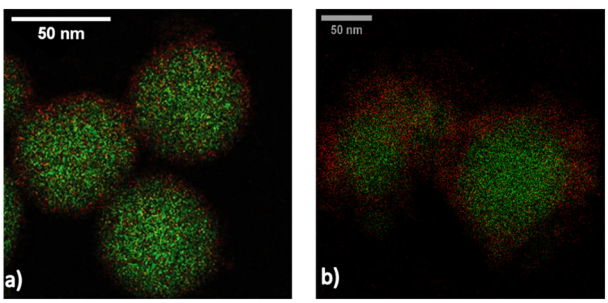

FIGURE 2 | STEM/EDX mapping of air passivated Ti^0 NPs **(a)** and SHT-treated at 164°C Ti@TiO_2 NPs **(b)**, green dots – Ti, red dots - O.

RESULTS AND DISCUSSION

Morphological and Structural Studies

TEM images depicted in **Figure 1A** reveal a quasi-spherical morphology of air passivated Ti particles with an average size of around 30–150 nm without any crystals at the surface. On the other hand, EDX mapping (**Figure 2a**) indicates the presence of oxygen-enriched layer at the surface of air-passivated Ti particles. This layer with a thickness about 11 nm is also clearly distinguishable in the HRTEM image of Ti NPs particles in **Figure 1A**. Sonohydrothermal treatment leads to the formation of nanocrystalline shell composed of 10–20 nm oxygen-enriched particles, however, formed core-shell particles preserve quasi-spherical morphology as it is displayed in **Figures 1B,C**, **2b**. We noticed that at the SHT temperature of about 100°C only few nanocrystals are formed, nevertheless their amounts increase with the increase of SHT temperature. The average particle size increases on ca. 5–10% after the coating with TiO_2 compared to initial Ti particles.

XRD diagram of air passivated Ti NPs in **Figure 3A** displays the patterns of metallic α-phase titanium (JCPDS 00-044-1294) with admixtures of tetragonal non-stoichiometric titanium hydride TiH_x (x = 1.53 – 1.97, JCPDS 01-079-6209) as it often observed in commercial titanium powders (Ageev et al., 1976). However, more thoughtful analysis of XRD data using Rietveld

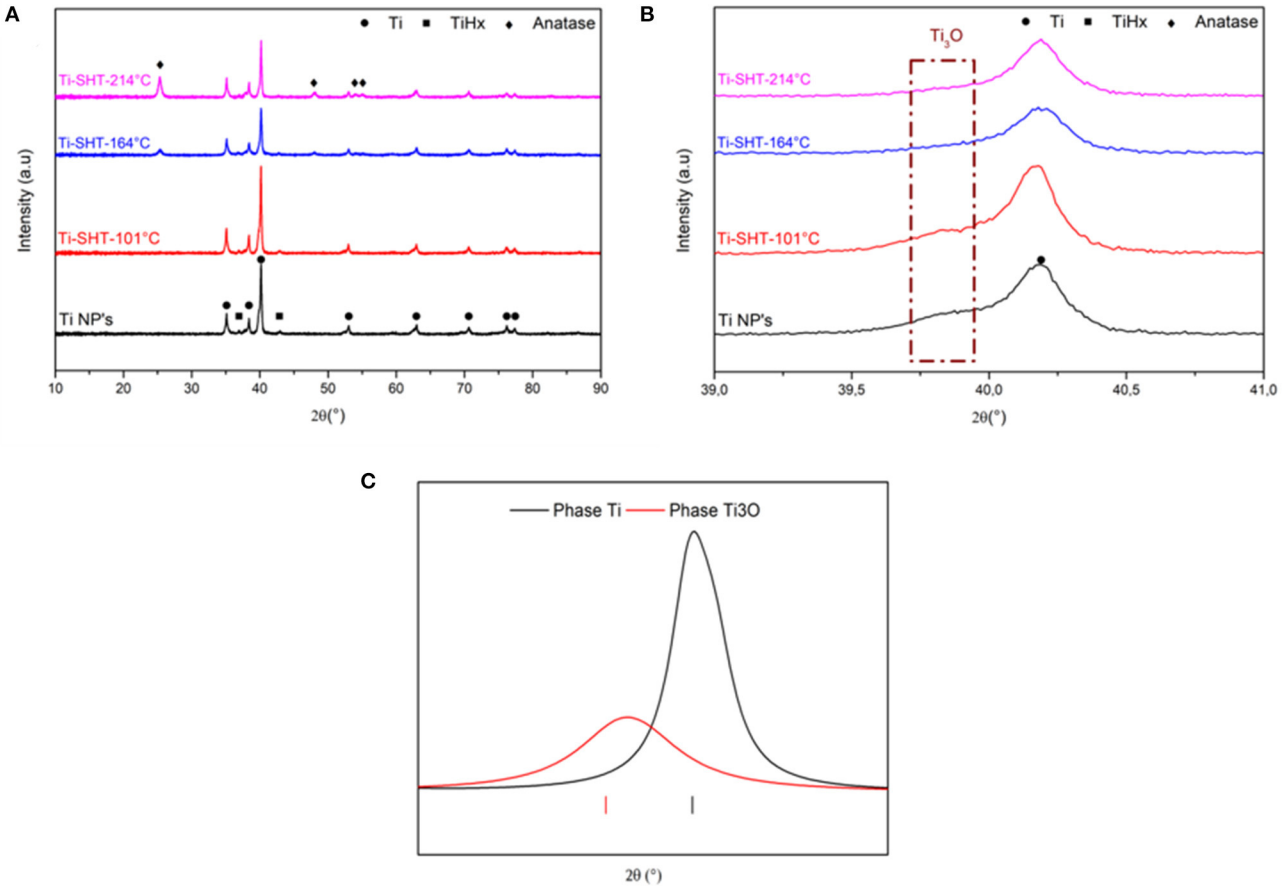

FIGURE 3 | XRD patterns of the initial Ti NPs and Ti@TiO_2 NPs treated at different temperatures under SHT conditions **(A)**. Zoom of the figure **(A)** in 39–41 2θ° range indicating the decrease in Ti_3O content with increasing of SHT temperature **(B)**. Example of Rietveld fit of the XRD diagram for Ti NPs in 39–41 2θ° range indicating the presence of Ti_3O phase **(C)**, red line – Ti_3O, black line – α-Ti.

refinement revealed the presence of scarce Ti_3O suboxide with $P\overline{3}1c$ space group symmetry (**Figures 3B,C**) (Yamaguchi, 1969). To the best of our knowledge, this is the first observation of Ti_3O phase at the nanoscale. It is worth noting that the XRD diagram of Ti NPs does not exhibit the presence of crystallized Ti(IV) oxides. The XRD data of the samples SHT treated at 164 and 214°C clearly point out drop of Ti_3O content and formation of TiO_2 anatase (JCPDS 00-021-1272), which is in line with HRTEM observations (**Figure 1B**).

High-resolution Ti 2p XPS spectra shown in **Figure 4** were fitted using binding energies published in the NIST database (Wagner et al., 2003). The XPS spectrum of air passivated Ti NPs revealed the presence of Ti^0 and lower oxidation states of titanium at the particle surface in agreement with the XRD analysis revealed the presence of titanium suboxide in Ti NPs. In contrast to XRD data, the XPS spectrum of Ti NPs also exhibits a signal typical for TiO_2 (**Figure 4A**). This discrepancy could be assigned to the formation of amorphous hydrated titanium oxide $TiO_2{\cdot}xH_2O$ at the surface of metallic titanium. SHT treatment causes disappearance of Ti^0, TiO, Ti_xO_y, and Ti_2O_3 peaks from the XPS spectrum and the experimental XPS spectrum of Ti@TiO_2 NPs can be fitted perfectly well by defect-free TiO_2 spectrum indicating effective coating of metallic titanium core (**Figure 4B**).

Table 1 summarizes the phase compositions of initial Ti particles and prepared materials obtained from the Rietveld refinement of powder XRD data. One can conclude that air passivated Ti NPs are stable during the SHT treatment until ca. 100°C. Further heating until ca. 150°C causes oxidation of Ti_3O to TiO_2:

$$Ti_3O + 5H_2O \rightarrow 3TiO_2 + 5H_2 \quad (1)$$

At higher temperature, metallic titanium is also oxidized yielding TiO_2:

$$Ti + 2H_2O \rightarrow TiO_2 + 2H_2 \quad (2)$$

According to the XPS data anatase nanocrystals at the surface of Ti NPs also can be formed by crystallization of $TiO_2{\cdot}xH_2O$ species. It is worth noting that SHT oxidation of Ti NPs is more effective than hydrothermal heating without ultrasound

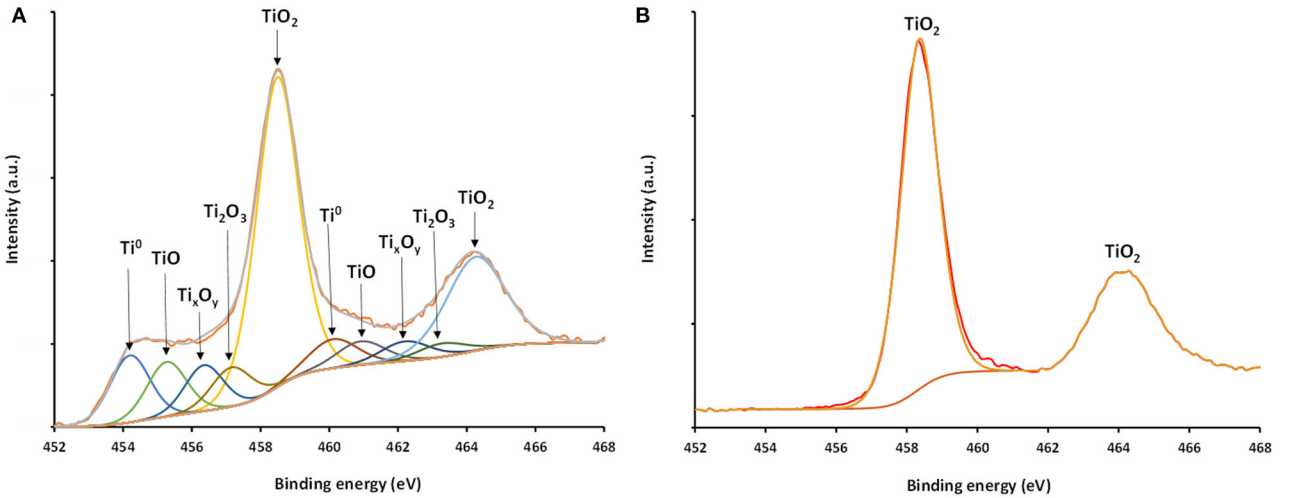

FIGURE 4 | Fitted Ti 2p high-resolution XPS spectra of air-passivated Ti^0 **(A)** and SHT/214°C Ti@TiO_2 **(B)** NPs. Red line indicates experimental spectrum.

TABLE 1 | Variation of Ti NPs composition with the temperature of SHT treatment obtained by Rietveld refinement of XRD patterns.

Sample	mol.% (±5%)		
	Ti	Ti_3O	TiO_2 anatase
Air passivated Ti*	86	14	–
SHT 101°C	88	12	–
HT 150°C**	88	5	7
SHT 164°C	≥80.5	≤1.5	18
SHT 214°C	≥62	≤3	35

Time of treatment was equal to 3 h.
**The admixture of TiH_x and amorphous $TiO_2{\cdot}xH_2O$ species were not taken into account.*
***HT stands for hydrothermal treatment without ultrasound. XRD and TEM data for these NPs are shown in **Supplementary Figure 3**.*

TABLE 2 | Thermal stability of Ti and Ti@TiO_2 NPs obtained from TGA analysis.

Sample	Air passivated Ti	SHT/101°C	SHT/164°C	SHT 214°C
T_{ox}±10°C	230	240	263	304

*T_{ox} indicates the begining of metallic titanium core oxidation calculated as it shown in **Supplementary Figure 4**.*

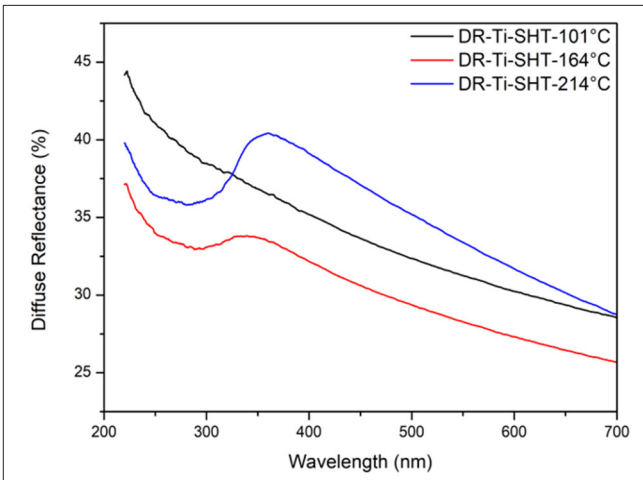

FIGURE 5 | Solid-state reflectance spectra of Ti^0 NPs before and after sonohydrothermal treatment at different temperatures. The spectrum of Ti particles SHT treated at 101°C is very similar to the spectrum of air-passivated Ti0 particles reported recently (Nikitenko et al., 2015).

(**Table 1**), which was attributed to better heat and mass-transfer in the case of SHT process due to the acoustic cavitation, i.e., formation, non-linear oscillations, and implosion of microbubbles formed in the hydrothermal water under the effect of ultrasonic waves (Cau et al., 2013). Results of TGA analysis displayed in **Supplementary Figure 4** and **Table 2** point out the increase of titanium metallic core thermal stability with the increase of SHT temperature, which is explained by the formation of protective TiO_2 shell. It should also be emphasized that the hydrothermal oxidation of micrometric titanium powder begins at much higher temperature of about 450°C (Yoshimura et al., 1989), which is most likely related to the particle size effect.

Light Absorption and Charge Transfer

All Ti-based materials studied in this work have intense black color indicating extented photoresponse with nearly full solar spectrum. The solid state reflectance spectra of both Ti and Ti@TiO_2 NPs (**Figure 5**) exhibit a broad band spanning from UV to NIR spectral range, which was attributed to intraband and interband transitions of metallic Ti (Gawande et al., 2015; Nikitenko et al., 2015). In addition, the spectra of Ti@TiO_2 NPs reveal an absorption band centered at 220–350 nm typical for the bandgap transition of crystallized TiO_2. Kubelka-Munk treatment of the spectral data using $(F(R)hv)^{1/2}$ *vs* E function

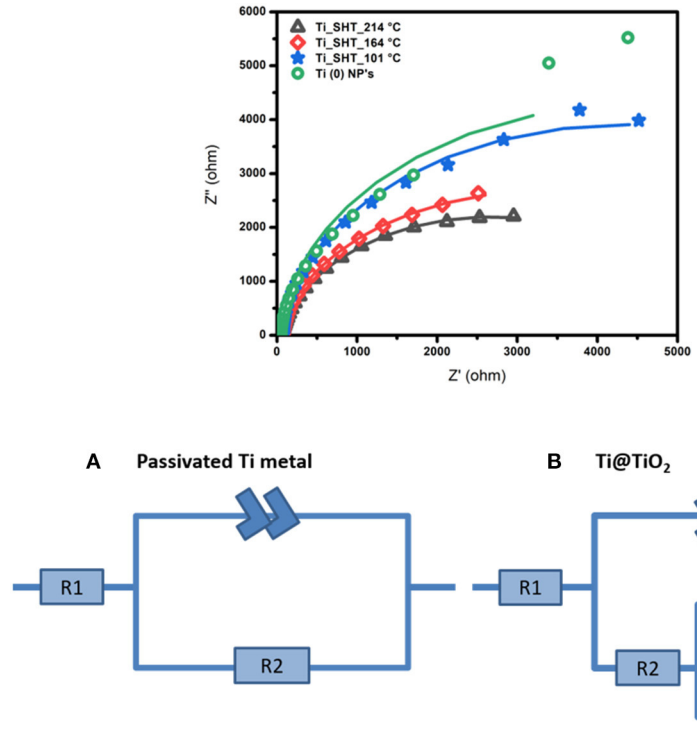

FIGURE 6 | Nyquist plots for Ti^0 NPs and $Ti@TiO_2$ NPs and the equivalent circuit for Ti^0 **(A)** and $Ti@TiO_2$ **(B)**.

(López and Gómez, 2012) shown in **Supplementary Figure 5** gives a bandgap energy value of 3.52 and 3.51 eV for SHT 164°C and SHT 214°C respectively, which is slightly greater than the bandgap energy reported for commercial anatase TiO_2 powder (E = 3.26 eV) (López and Gómez, 2012). This difference may originate from the overlap of Ti^0 interband/intraband transitions and TiO_2 bandgap in the UV spectral range (**Figure 5**). Kubelka-Munk treatment could lead to the overestimated value of the bandgap energy in this case.

The electrochemical impedance spectroscopy (EIS) provides a valuable information about the charge transfer and charge recombination processes at the interface of the catalysts and electrolytes (Barsoukov and Macdonald, 2005). **Figure 6** shows the Nyquist plots and the proposed equivalent circuits of the passivated Ti NPs and $Ti@TiO_2$ NPs obtained after SHT at 101, 164, and 214°C. The reduced size of semicircles indicates a lower charge transfer resistance at the particle/electrolyte interface. Surprisingly, Ti particles coated with TiO_2 nanocrystals exhibit more effective electron transfer than air-passivated Ti NPs or Ti NPs treated at 101°C with very low content of TiO_2 NPs at the Ti metal surface. The resistances calculated for equivalent circuits are summarized in the **Table 3**. The R_1 refers to the bulk resistance of electrodes and electrolytes, and R_2 represents the resistance at the interface of the particles and electrolytes. A third resistance R_3 is only observed for $Ti@TiO_2$ NPs and is most likely related to the second interface formed between TiO_2 nanoparticles from the shell and Ti^0 core. Interesting that R_3 increases with the temperature of SHT treatment, or, in other words, with the increase of TiO_2 anatase content. High R_2 value (9.05 kΩ) for Ti^0 NPs most probably is attributed to the passivating layer at the metal surface leading to the hindering of charge transfer. Among $Ti@TiO_2$ NPs, the sample obtained at 214°C displays the lowest R_2 value indicating the fastest charge transfer rate for this material. This conclusion is in an agreement with an effective charge separation in $Ti@TiO_2$ NPs recently demonstrated using photoluminescence spectroscopy (Nikitenko et al., 2018).

TABLE 3 | EIS parameters for Ti and $Ti@TiO_2$ NPs.

Samples	R_1 (Ω)	R_2 (Ω)	R_3 (kΩ)
$Ti@TiO_2$ SHT 214°C	59.95	7.96	5.44
$Ti@TiO_2$ SHT 164°C	48.63	22.85	7.67
$Ti@TiO_2$ SHT 101°C	42.06	34.03	9.12
Air passivated Ti NPs	49.84	9.05 (kΩ)	not been observed

Photocatalytic Hydrogen Production

Typical hydrogen emission profiles and calculated H_2 yields for studied photocatalysts shown in **Figure 7** highlight the crucial role of TiO_2 nanocrystalline shell in the reaction of photocatalytic glycerol reforming. Kinetic data reveal a clear relationship between the temperature of SHT treatment, or, in other words, between anatase content in $Ti@TiO_2$ NPs, and H_2 yield (**Figure 7B**). In addition, photocatalytic activity correlates

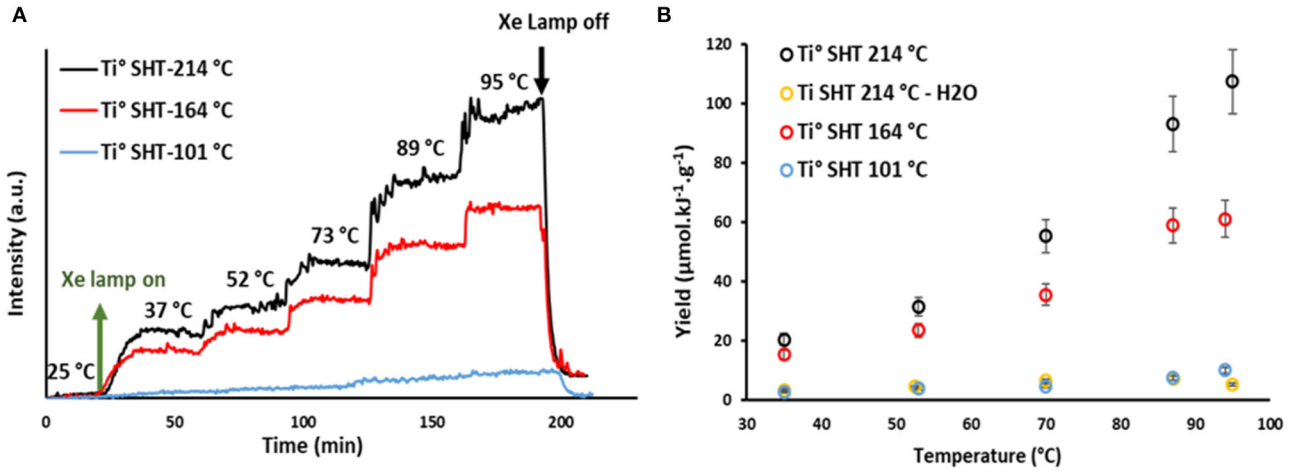

FIGURE 7 | Typical hydrogen emission profiles with catalysts obtained at 101, 164, and 214°C SHT temperatures in solutions of 0.5 M glycerol under Xe-lamp white light and Ar flow **(A)**, and H_2 yields in 0.5 M glycerol solutions and pure water for SHT-214°C catalyst **(B)**. The uncertainty for H_2 yields was estimated about 10–15%.

with EIS data exhibiting more effective charge transfer for SHT 214°C NPs. The role of TiO_2 in the reaction mechanism can be understood in terms of the charge separation between semiconducting TiO_2 shell and metallic Ti^0 core. The optical spectra (**Figure 5**) show that the incident light of the Xe lamp in UV/vis/NIR spectral range is mainly absorbed by Ti^0 core. In non-plasmonic metal, such as titanium, electron-hole pairs can be created by interband transitions via non-radiative Landau damping mechanism (Kale et al., 2014). However, in a highly conducting, metallic material, the electron-hole recombination would be extremely rapid in the absence of hole and/or electron scavengers. Therefore, one might suggest that in Ti@TiO_2 core-shell NPs TiO_2 provides effective charge separation, what was confirmed by fluorescence spectroscopy in previous study (Nikitenko et al., 2018). In addition, TiO_2 can absorb at least part of the UV incident light followed by electron-hole pairs generation in semiconducting particle. In this case, charge separation would be provided by electron migration to Ti^0 core, as it occurs in TiO_2 photocatalyst loaded with noble metal nanoparticles (Ma et al., 2014; Ghosh, 2018).

Furthermore, photocatalytic process with Ti@TiO_2 NPs exhibits strong photothermal effect in an agreement with our previous results (Nikitenko et al., 2018). **Figure 7B** demonstrates that the yield of H_2 increases in ca. 4 times when the bulk temperature increases from 37 to 95°C. On the other hand, in dark conditions formation of H_2 is not observed even at 95°C indicating the photonic origin of studied process. Kinetics of H_2 formation obeys an Arrhenius law (**Supplementary Figure 6**) and the calculated apparent activation energy, E_{act}, for found to be equal to 31 ± 5 and 25 ± 5 kJ·mol^{-1} for SHT 164°C and SHT 214°C, respectively. It is worth noting that these values are much lower than the typical activation energy of chemical bonds and has been previously assigned to the diffusion of intermediates at the catalyst surface (Nikitenko et al., 2018). Alternatively, the temperature dependence of photocatalytic reactions can be also related to the dynamics of water adsorbed at the surface of the catalyst (E_{act} = 16–21 kJ·mol^{-1}, Parrino et al., 2017).

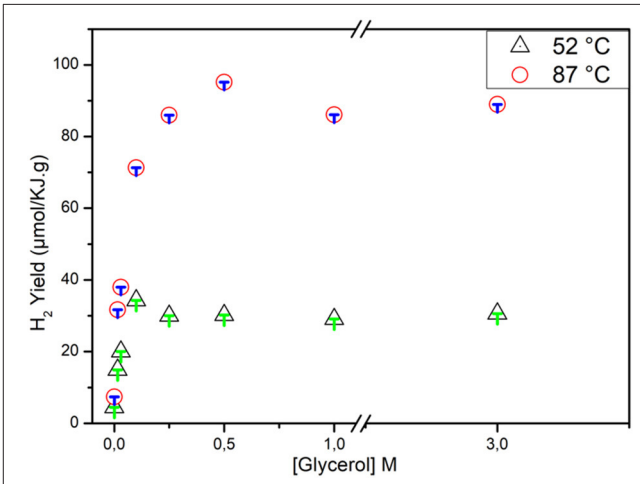

FIGURE 8 | Plot of the H_2 formation yields against glycerol concentrations over SHT 214°C Ti@TiO_2 photocatalyst at 53 and 87°C.

Figure 8 shows the influence of glycerol concentration on H_2 formation with the most active SHT 214°C Ti@TiO_2 photocatalyst. The yield of H_2 increases with the glycerol concentration and then levels off at [Glycerol] ≥ 0.5 M in an agreement with Langmuir-type function indicating that the mechanism of photocatalytic process involves glycerol adsorption at the active sites of the catalyst. Similar behavior has been reported for photocatalytic glycerol reforming over Pt/TiO_2 (Jiang et al., 2015) and NiO/TiO_2 (Fujita et al., 2016) NPs. On the other hand, kinetics with Ti@TiO_2 NPs reveals H_2 emission even from pure water at elevated temperature (**Supplementary Figure 7**). This observation is

largely in agreement with the above conclusion that both water and glycerol can contribute to the observed photothermal effect.

Mass spectrometric measurements indicate the absence of CO_2 emissions (**Supplementary Figure 8**) during the photothermal process with glycerol in consonance with our previous study (Nikitenko et al., 2018). It is worth noting that photocatalytic glycerol reforming in the presence of nanocrystalline P25 TiO_2 (83% of anatase and 17% of rutile) leads to CO_2 and CO formation (Liu et al., 2014), which implies a certain difference in reaction mechanisms with $Ti@TiO_2$ and TiO_2 photocatalysts. We found that in studied system H_2 formation is accompanied by acidification of photolyte from pH = 6 to pH = 4 in a ca. 3 h of photolysis indicating formation of some acidic products without decarboxylation. It has recently been suggested that glycerol is oxidized to glyceric acid in the studied process (Nikitenko et al., 2018). In addition, it is known that the wet catalytic oxidation of glycerol can also lead to the formation of other carboxylic acids without decarboxylation, such as tartronic acid, mesooxalic acid, and hydroxypyruvic acid (Worz et al., 2009).

On the basis of the above data, it can be concluded that the mechanism of H_2 formation in studied system involves two reaction pathways illustrated in **Figure 9**: splitting of water molecules (Equations 3–5 presuming four-electron process) and glycerol reforming (Equations 6–12):

H_2O splitting:

$$Ti@TiO_2 + H_2O \rightleftarrows Ti@TiO_2{\cdot}H_2O \quad (3)$$

$$Ti@TiO_2{\cdot}H_2O + h\nu \rightarrow [^{e}Ti@TiO_2^{h+}]{\cdot}H_2O \quad (4)$$

$$[^{e}Ti@TiO_2^{h+}]{\cdot}H_2O \rightarrow Ti@TiO_2 + H_2 + 1/2O_2 \quad (5)$$

Glycerol reforming:

$$Ti@TiO_2 + RCH_2OH \rightleftarrows Ti@TiO_2{\cdot}RCH_2OH \quad (6)$$

$$Ti@TiO_2{\cdot}RCH_2OH + h\nu \rightarrow [^{e}Ti@TiO_2^{h+}]{\cdot}RCH_2OH \quad (7)$$

$$RCH_2OH + 2h^+ \rightarrow RCHO + 2H^+ \quad (8)$$

$$2H^+ + 2e^- \rightarrow H_2 \quad (9)$$

$$RCHO + H_2O \rightarrow RCH(OH)_2 \quad (10)$$

$$RCH(OH)_2 + 2h^+ \rightarrow RCOOH + 2H^+ \quad (11)$$

$$2H^+ + 2e^- \rightarrow H_2 \quad (12)$$

where RCOOH in the Equation (11) could represent a mixture of mentioned above carboxylic acids. It is worth mentioning that the direct water splitting is practically observable at the sufficiently high temperature only. In general, higher yield of hydrogen for glycerol compared to water was attributed to more effective hole scavenging by glycerol than by water (Jiang et al., 2015, Tang et al., 2008). The link between surface charge carrier dynamics and photocatalytic activity of $Ti@TiO_2$ NPs is in line with this conclusion.

Finally, the stability of $Ti@TiO_2$ photocatalysts at studied conditions was tested using HRTEM and ICP-OES techniques. Modification of the particle's morphology was not detected by HRTEM after photothermal experiments as shown in **Supplementary Figure 9**. ICP-OES analysis has been performed

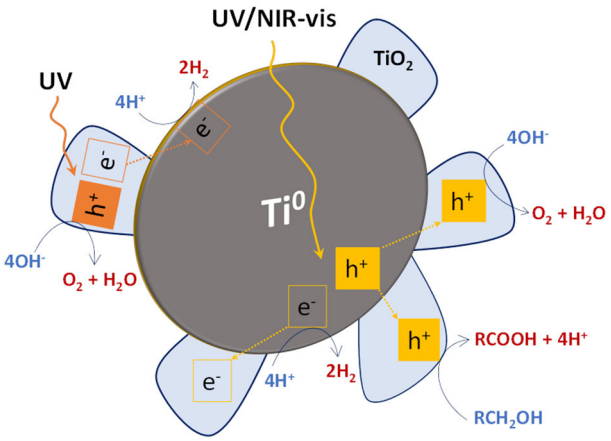

FIGURE 9 | Graphical sketch of suggested mechanism of H_2 photocatalytic formation in the presence of $Ti@TiO_2$ core-shell nanoparticles.

with SPECTRO ARCOS instrument (detection limit of titanium was ca. 0.1 ppm). Particles of catalyst have been removed from the reaction mixture by filtration through 0.2 μm PTFE filter prior analysis. The ICP-OES analysis after 8 h of photocatalytic experiments in hot 0.5 M glycerol solutions revealed a leak of about 0.09 and 0.29% of titanium for SHT 214°C and SHT 164°C $Ti@TiO_2$ NPs, respectively.

CONCLUSIONS

In summary, this work provides some new insights into the structure and thermally-assisted photocatalytic properties of Ti^0 and $Ti@TiO_2$ nanoparticles. Rietveld refinement of XRD data revealed the presence of scarce titanium suboxide Ti_3O with a $P\overline{3}1c$ space group symmetry in raw α-Ti^0 NPs. According to STEM/EDX study this species is situated at the surface of Ti^0 NPs. Formation of the species with lower oxidation states of titanium was also observed by XPS spectroscopy. Our results confirm previous conclusion (Kornilov et al., 1970) about Ti_3O stability at room temperature. Sonohydrothermal synthesis allows to control nanocrystalline TiO_2 shell in $Ti@TiO_2$ NPs using pure water as a solvent. Mechanism of TiO_2 shell formation depends on the SHT temperature: in the temperature range 100–150°C TiO_2 is formed mainly by the oxidation of Ti_3O, and oxidation of Ti^0 to TiO_2 occurs at higher temperature. Coating of titanium metal nanoparticles with anatase nanocrystals provides their better stability to oxidation and strong photothermal effect of hydrogen production from aqueous glycerol solutions. In a hot water, photocatalytic formation of hydrogen is observed even without glycerol. However, the yield of hydrogen in the presence of glycerol is higher than that in pure water, which can be related to more effective scavenging of photogenerated holes with glycerol. Glycerol reforming leading to hydrogen production is not accompanied by CO_2 emission in studied system. The acidification of the photolyte solution implies that glycerol is oxidized to some acidic products, most probably, to

the mixture of organic acids derived from glycerol. The apparent activation energy $E_{act} = (25–31) \pm 5$ kJ·mol^{-1} of studied process is much lower than the typical activation energy of chemical bonds indicating that the origin of the photothermal effect is related to the diffusion of intermediates arise from glycerol or from the dynamics of water adsorbed at the surface of the catalyst.

DATA AVAILABILITY STATEMENT

The original contributions presented in the study are included in the article/**Supplementary Material**, further inquiries can be directed to the corresponding author.

AUTHOR CONTRIBUTIONS

SN and SR conceived the study. SN, SR, TC, and SE prepared the manuscript. TC and SE prepared the samples and performed their characterization. SE and SN performed photocatalytic experiments. AN and SE performed electrochemical study. All authors contributed to this work and approved the submitted version.

FUNDING

This work has been partially funded by the CNRS Energy unit (Cellule Energie) through the project PHOTOCAT.Ti@TiO2.H2.

ACKNOWLEDGMENTS

The authors kindly acknowledge Dr. Adel Mesbach for Rietveld refinement of XRD data, Dr. Xavier Le Goff for HRTEM measurements, Dr. Cyrielle Rey for TGA measurements, and Dr. Valerie Flaud for XPS analysis.

SUPPLEMENTARY MATERIAL

The Supplementary Material for this article can be found online at: https://www.frontiersin.org/articles/10.3389/fctls.2021.669260/full#supplementary-material

REFERENCES

Ageev, N. V., Babareko, A. A., Rubina, E. B., Betsofen, S., Ya., and Bunin, L. A. (1976). X-ray diffraction analysis of titanium hydrides in commercial titanium alloys. *Met. Sci. Heat Treat.* 18, 124–130. doi: 10.1007/BF00664146

Barsoukov, E., and Macdonald, J. R. (eds.). (2005). Impedance Spectroscopy: *T*heory, *E*xperiment, and *A*pplications. Hoboken, NJ: Wiley-Interscience. doi: 10.1002/0471716243

Baykara, S. Z. (2018). Hydrogen: a brief overview on its sources, production and environmental impact. *Int. J. Hydrogen Energy* 43, 10605–10614. doi: 10.1016/j.ijhydene.2018.02.022

Cau, C., Guari, Y., Chave, T., Larionova, J., Pochon, P., and Nikitenko, S. I. (2013). Sonohydrothermal synthesis of nanostructured (Ce,Zr)O_2 mixed oxides with enhanced catalytic performance. *J. Phys. Chem. C* 117, 22827–22833. doi: 10.1021/jp407096p

Fujita, S.-I., Kawamori, H., Honda, D., and Arai, M. (2016). Photocatalytic hydrogen production from aqueous glycerol solution using NiO/TiO_2 catalysts: effects of preparation and reaction conditions. *Appl. Cat. B Environ.* 181, 818–824. doi: 10.1016/j.apcatb.2015.08.048

Gawande, M. B., Goswami, A., Asefa, T., Guo, H., Biradar, A. V., Peng, D.-L., et al. (2015). Core–shell nanoparticles: synthesis and applications in catalysis and electrocatalysis. *Chem. Soc. Rev.* 44, 7540–7590. doi: 10.1039/C5CS00343A

Ghosh, S. (2018). *Visible-Light-Active Photocatalysis: Nanostructured Catalyst Design, Mechanisms and Applications*. Mörlenbach: Wiley-VCH. doi: 10.1002/9783527808175

Jiang, X., Fu, X., Zhang, L., Meng, S., and Chen, S. (2015). Photocatalytic reforming of glycerol for H_2 evolution on Pt/TiO_2: fundamental understanding the effect of co-catalyst Pt and the Pt deposition route. *J. Mater. Chem.* 3, 2271–2282. doi: 10.1039/C4TA06052K

Kale, M. J., Avanesian, T., and Christopher, P. (2014). Direct photocatalysis by plasmonic nanostructures. *ACS Catal.* 4, 116–128. doi: 10.1021/cs400993w

Kornilov, I. I., Vavilova, V. V., Fykin, L. E., Ozerov, R. P., S. P., Soloviev, S. P., et al. (1970). Neutron diffraction investigation of ordered structures in the titanium oxygen system. *Metal. Mater. Trans. B* 1, 2569–2571.

León-Reina, L., García-Maté, M., Álvarez-Pinazo, M. G., Santacruz, I., Vallcorba, O., De la Torre, A. G., et al. (2016). Accuracy in rietveld quantitative phase analysis: a comparative study of strictly monochromatic Mo and Cu radiations. *J. Appl. Cryst.* 49, 722–735. doi: 10.1107/S1600576716003873

Liu, R., Yoshida, H., Fujita, S.-I. M., and Arai, M. (2014). Photocatalytic hydrogen production from glycerol and water with NiO_x/TiO_2 catalysts. *Appl. Cat. B Environ.* 144, 41–45. doi: 10.1016/j.apcatb.2013.06.024

López, R., and Gómez, R. (2012). Band-gap energy estimation from diffuse reflectance measurements on sol–gel and commercial TiO_2: a comparative study. *J. Sol-Gel Sci. Technol.* 61, 1–7. doi: 10.1007/s10971-011-2582-9

Ma, R., Sun, J., Li, D. H., and Mei, J. J. (2020). Review of synergetic photo-thermo-catalysis: mechanisms, materials and applications. *Int. J. Hydrogen Energy* 45, 30288–30324. doi: 10.1016/j.ijhydene.2020.08.127

Ma, Y., Wang, X., Jia, Y., Chen, X., Han, H., and Li, C. (2014). Titanium dioxide-based nanomaterials for photocatalytic fuel generations. *Chem. Rev.* 114, 9987–10043. doi: 10.1021/cr500008u

Nikitenko, S. I., Chave, T., Cau, C., Brau, H.-P., and Flaud, V. (2015). Photothermal hydrogen production using noble-metal-free Ti@TiO_2 core-shell nanoparticles under visible-NIR light irradiation. *ACS Catal.* 5, 4790–4795. doi: 10.1021/acscatal.5b01401

Nikitenko, S. I., Chave, T., and Le Goff, X. (2018). Insights into the photothermal hydrogen production from glycerol aqueous solutions over noble metal-free Ti@TiO_2 core-shell nanoparticles. *Part. Part. Syst. Charact.* 35:1800265. doi: 10.1002/ppsc.201800265

Parrino, F., Conte, P., De Pasquale, C., Laudicina, V. A., Loddo, V., and Palmisano, L. (2017). Nature of interactions at the interface of two water-saturated commercial TiO_2 polymorphs. *J. Phys. Chem. C* 121, 2258–2267. doi: 10.1021/jp400298m

Shimura, K., and Yosida, H. (2011). Heterogeneous photocatalytic hydrogen production from water and biomass derivatives. *Energy Environ. Sci.* 4, 2467–2481. doi: 10.1039/c1ee01120k

Tang, J., Durrant, J. R., and Klug, D. R. (2008). Mechanism of photocatalytic water splitting in TiO_2. Reaction of water with photoholes, importance of charge carrier dynamics, and evidence for four-hole chemistry. *J. Am. Chem. Soc.* 130, 13885–13891. doi: 10.1021/ja8034637

Wagner, C. D., Naumkin, A., Kraut-Vass, A., Allison, J. W., Powell, C. J., and Rumble, J. R. (2003). *NIST Standard Reference Database 20, Version 3.4*. Available online at: http:/srdata.nist.gov/xps/.

Worz, N., Brandner, A., and Claus, P. (2009). Platinum–bismuth-catalyzed oxidation of glycerol: kinetics and the origin of selective deactivation. *J. Phys. Chem. C* 114, 1164–1172. doi: 10.1021/jp909412h

Yamaguchi, S. (1969). Interstitial order-disorder transformation in the Ti-O solid solution. I. Ordered arrangement of oxygen. *J. Phys. Soc. Jpn* 27, 155–163. doi: 10.1143/JPSJ.27.155

Yoshimura, M., Ohira, H., and Somiya, S. (1989). "Formation of TiO_2 and ZnO powders by hydrothermal oxidation of Ti and Zn metals," in *Hydrothermal Reactions for Materials Science and Engineering*, ed S. Somiya (Dordrecht: Springer), 112–125. doi: 10.1007/978-94-009-0743-0_17

Conflict of Interest: The authors declare that the research was conducted in the absence of any commercial or financial relationships that could be construed as a potential conflict of interest.